Development and evaluation of an automatic connection device for electric cars with four DOFs and a control scheme based on infrared markers

Jens Bucher*, Jan Knipschild and Bernd Künne

Department of Machine Elements,
TU Dortmund University,
Dortmund, Germany
Email: jens.bucher@tu-dortmund.de
Email: jan.knipschild@tu-dortmund.de
Email: bernd.kuenne@tu-dortmund.de
*Corresponding author

Abstract: The topic of electro mobility has become more and more present over the last few years. To increase the acceptance within the population, the continuous expansion of the charging infrastructure is immensely important. In this paper a developed cost efficient charging robot is presented, with only four actively controlled DOFs and an installed low cost camera in the CCS connector. The control scheme is based on using infrared LEDs inside the inlet, which reduce the influence of external light and reflections. The described plugging process includes the pose estimation and pre-positioning, a plausibility and identification check, visual servoing and the plugging/unplugging. Finally, the workspace is examined. Afterwards the developed elastic compensation unit of the robot is analysed for its capabilities to compensate angular deviations. In addition, the reaction forces and torques are measured. In summary in the pluggable workspace a plugging success rate of 97% can be achieved.

Keywords: automatic connection device; ACD; charging robot; electric vehicle; elastic compensation unit; CCS Combo 2; identification check; plausibility check; robot control scheme; infrared markers; visual servoing.

Reference to this paper should be made as follows: Bucher, J., Knipschild, J. and Künne, B. (2021) 'Development and evaluation of an automatic connection device for electric cars with four DOFs and a control scheme based on infrared markers', *Int. J. Mechatronics and Automation*, Vol. 8, No. 4, pp.175–186.

Biographical notes: Jens Bucher received his Master in Mechanical Engineering at the TU Dortmund University in 2018 and since that time he has been working as a research assistant at the Department of Machine Elements. His research focuses on robotics and large volume 3D printing.

Jan Knipschild received his Master in Mechanical Engineering at the TU Dortmund University in 2018 and since that time he has been working as a research assistant at the Department of Machine Elements. His research focuses on large volume 3D printing and robotics.

Bernd Künne has been a University Professor and the Head of the Department of Machine Elements at the TU Dortmund University since 1993. He has published several research papers at national and international journals, conference proceedings as well as several books and chapters of books.

1 Introduction

The increasing efforts to further reduce CO_2 emissions continue to push the development of electric vehicles. Due to the shorter range of the most vehicles, the lack of charging infrastructure and the high purchase price, the vehicle with combustion engine is usually preferred following the discussion of Mönnig et al. (2019). In order to enhance the comfort of the charging process and to enable people with physical limitations to use it without restrictions, a fully automatic charging process is required. In addition, the automatic charging process provides the basis for fully autonomous driving in the future.

There are already various approaches to charge an electric vehicle (EV) automatically. Some of them aim for charging at the bottom of the vehicle like DAZEPLUG (2019) or Easelink (2020). This has disadvantages such as possible accumulation of dirt or increased contact with road

salt and other external influences. Furthermore significant modifications to the vehicle are necessary. Because of these disadvantages, this paper proposes a charging system that is able to charge an EV conductively from the side eliminating the need of an additional charging port.

Previous concepts are often based on industrial robots with six or seven active controlled axes such as the developed concept by Innogy SE (2019) or the concept for fleet vehicles made by Electrify America (2019). Any technical details about their plugging process such as repeatability, reliability or visual control procedures have not yet been published. These robots are expensive and furthermore, three rotational degrees of freedom (DOF) are not required for an ideally positioned EV with respect to the charging station. The second category is a mobile charging system consisting of an automatic connection device (ACD) and a battery mounted on a movable chassis. The mobile charging system itself is charged at a stationary charging station and drives to an EV. Finally, it charges from the internal battery. Charging stations belonging in this category are Samsungs's robot unit (EVAR, 2018) and the developed prototype (CarLa, 2018) by *Volkswagen AG*. The third category of bionic concepts includes the snake-like kinematics of Tesla referred in the conference paper of the 16th International Stuttgart Symposium by Walzel et al. (2016). Again, no technical data and evaluations have been published until now. A related design was developed by Lou and Di (2020) using a cable-driven robot with four DOFs and an elastic compensation unit at the connector. The four DOF are provided by three rotational and one translational axis, which are driven by six cable pulls and a linear moving platform. Therefore, at least seven actively controlled actuators are required. Another kinematic system that reminds of a human arm rotated by 90° is the KUKA CarLa Connect (2020) charging robot with five actively controlled axes and four DOFs. Unfortunately no technical details concerning the image processing or robot control scheme have been published.

The research project 'ALanE' at the TU Dortmund University already tested automated lateral charging using a prototype robot and visual servoing as shown by Wissing et al. (2015). This connecting device has only three actively controlled axes and the connector is kept aligned horizontally. But initial results have already shown that the use of an elastic compensation unit in addition to three DOFs is sufficient for plugging. The disadvantage is that the used robot with a fixed connector orientation is only able to plug into angled inlets with high forces and a lot of elastic compensation while the reliability decreases with increasing angle. Common connector manufacturers like Phoenix Contact GmbH & Co. KG (2020) specify less than 100 N as the permitted insertion force by hand. In addition the ACD can be characterised as dangerous for public spaces due to its scissor kinematics and the absence of sensors.

Besides the mechanics of the charging robot, the detection of the inlet and the estimation of its pose are essential for the successful automatic plugging. Various approaches are suitable for image-based inlet detection. One opportunity is trying to identify the contour without adding any markers to the inlet. With an edge detection, it is possible to detect the inlet due to its characteristic shape. Using of a high-resolution camera in the connector (eye-in-hand) of the robot arm or beside the robot (eye-to-hand), which detects the inlet and performs a matching, it is on the one hand very expensive and on the other hand computationally intensive. An example for a template matching using the Halcon Machine Vision software is shown and evaluated by Miseikis et al. (2017). The experiments demonstrate that plugging is basically possible, but that frequent misalignments between connector and inlet also occur. Hence the connector is sometimes not fully inserted. In addition, these misalignments can lead to high forces on the inlet and connector, which were not evaluated in their experiments. It can also be assumed that the image processing is very sensitive to undesired light influences such as reflections or external light sources. One more example in which a template matching is used comes from Behl et al. (2019) where a mobile autonomous robot travels to the inlet for charging. Quan et al. (2021) do not use additional markers on the inlet either. They develop an image processing based on contour information. The experiments in different lighting conditions indoors and outdoors show that more than 90% can be plugged successfully. However, problems are also identified with uneven lighting conditions and a high light intensity. Alternatively, using of a neural networks to detect the inlet is becoming increasingly popular. Pan et al. (2020) show that a detection is successful even at high light intensity. However, the training of neural networks is computationally intensive and takes a lot of time.

A second approach for detecting the inlet is to use a marker such as placing a label on the inlet. Due to the texture less black plastic material, it is difficult to find good features on the inlet according to Lv et al. (2019), especially when using a monocular camera. For this reason Lv et al. (2019) are using an attached rectangular label on the inlet cover. This enables the using of the SURF algorithm by Bay et al. (2008) for label detection. Finally, the relative pose of the camera to the label is calculated using a perspective-n-point (PnP) algorithm based on the four corner points of the label. First tests under laboratory conditions demonstrate that it is possible to plug in. However, the tilt angle of the cover was assumed to be known. Alternatively to a label a QR code can be used as Taraglio (2017) presents for the automatic charging of buses. In this case, the QR code is very large what is probably not easily applicable for a car inlet. As shown by Harik (2021) using of another fiducial marker for an automatic charging system for agricultural electrical vehicles is also applicable.

A third variant for detecting the charging pose is using actively controllable markers, such as infrared (IR)-LEDs which can be switched on and off. Using IR markers was already investigated by Petrov et al. (2012) and Pérez et al. (2013). There, the car was equipped with a camera, so the car positioned itself accordingly to the charging station following the IR markers. First approaches with IR markers

in the car inlet were already designed for the prototype of the TU Dortmund University as described by Wissing et al. (2015).

In this article the development of a cost effective charging robot with four DOFs and a robust control scheme that can be classified as safe in public places is described first (Sections 2 and 3). The approach to reduce the robot costs is to develop a concept that has a small number of actively controlled axes and actuators. Nevertheless, in case of position deviations, which cannot be corrected with the existing DOFs, plugging should be possible without problems. An approach is based on an intended compliance that is sufficient to compensate for the positional deviations that occur when parking in a single parking space. The compliance makes position control impossible and requires a visual servoing. Besides the kinematics the second main aspect of this paper is the evaluation of an image-based approach with IR-LEDs in the car inlet as markers and a low-cost camera in the connector. Using of IR-LEDs and a camera with an attached IR-pass filter, reduces the necessary image editing processes and increases the robustness against external light influences like sunlight or external light sources and reflections as well. Even at night plugging is possible without an extra light source. In addition, a wireless communication between EV and charging station enables incorrect pairing. The LEDs offer the possibility of a visual assignment check between the EV and charging station.

Finally, in Section 4 is presented in which position range a reliable plugging with the developed ACD and the Combo 2 connector is possible and which inlet orientations can be plugged successfully without the missing DOFs. The Combo 2 connector is not a circular connector and shows only a limited self-centring property what makes the automatic plugging difficult. The evaluation is based on several test series.

2 ACD design

For the charging process, the vehicle has to be parked parallel to the charging station. Due to the fact that several vehicles from different manufacturers have the inlet positioned at various positions at the chassis, the charging robot has to be able to travel parallel to the vehicle. Positioning errors along the vehicle axis during the parking process can be compensated as well. Furthermore, the tilt angle of the inlet can be different. This is why it has to be possible to tilt the connector and execute a linear movement into the inlet for plugging.

Figure 1(a) shows the ACD kinematics with four actively controlled axes. The ACD is mounted on a wall parallel to the direction of travel. The first axis is a linear one for the parallel movement and is mounted closely to the wall. The axes two and three are rotational and cover the two missing translational DOFs. The rotational fourth axis is to control the angle around the x-axis in the world coordinates. The remaining rotational DOFs around the y- and z-axis cannot be actively controlled. In case of such angular misalignments between the vehicle and the charging robot, an elastic compensation system has to be installed to allow the self alignment of the connector.

Figure 1 Development of the ACD, (a) kinematic concept: 1 – linear, 2 – rotating, 3 – rotating and 4 – rotating (b) ACD design: i – shoulder, ii – upper arm, iii – forearm and iv – head unit (c) home position (d) ACD assembled: i – linear axis, ii – shoulder, iii – upper arm, iv – forearm and v – head (see online version for colours)

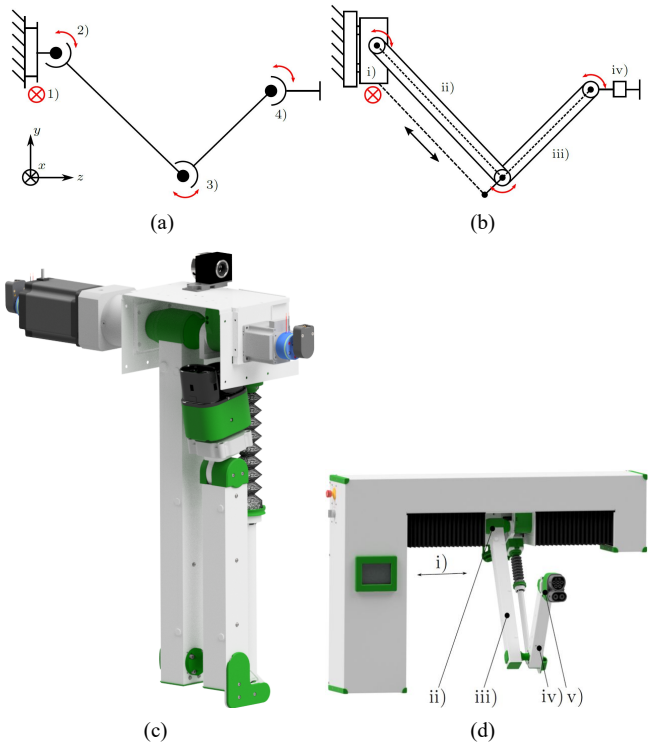

Figure 1(b) shows the ACD design. It is evident that the robot design belongs to the third category of bionic concepts. The robot arm is designed like a human arm and consists of the shoulder, the upper arm and the forearm. The connector is rotary mounted to the forearm. A linear axis i runs through the shoulder and allows the robot to operate on a linear guide. The upper arm ii is rotated by an actuator located in the shoulder axis. The forearm iii is moved by a lead screw that engages the elbow by a lever. The head angle iv can be adjusted via a toothed belt passing through the upper arm and forearm. The feed-through prevents the danger of crushing by the belt. By locating the motors in the shoulder of the robot, the mass of the robot arm is reduced. A reduced moving mass increases safety against injuries in case of collision.

The minimum distances between moving parts, according to ISO 13854, are taken into account for the design. In combination with motor current monitoring it guarantees safety from crushing injuries and ensures safe operation. Figure 1(c) shows the robot arm in its home position and Figure 1(d) displays the complete wall mounted design of the charging robot. The linear axis movement is encapsulated with the aid of a slide way protector against external influences and for protection

against human interference. The linear spindle for moving the forearm is also protected by a gaiter. The belt is fed through hollow shafts and enables the rotary movement of the Combo 2 connector.

Figure 2 Connector and the elastic compensation unit, (a) side view from connector (b) elastic compensation unit (see online version for colours)

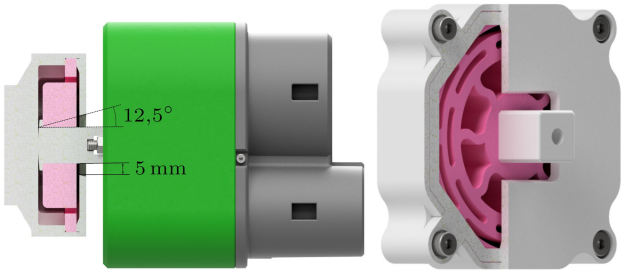

(a) (b)

For the development of the elastic compensation unit, the requirements are identified by Bergmann (2015). In this work an industrial robot with a mounted CCS Combo 2 connector plugs into an inlet that is spring-mounted in a cardanic suspension. This allows the inlet to align itself, even if the connector is not optimally aligned to in the Inlet. The results of the measured deviations are shown in the Table 1 [related to the inlet coordinate system in Figure 3(b)]. It is noticeable that the angular tolerance for θ_x is not the same in both directions of rotation. This is due to the asymmetrical shape of the inlet. The two remaining directions of rotation θ_y and θ_z show a symmetrical behaviour. For the translational part, a maximum elastic compensation of 5 mm is selected so that the entire required range is covered. Since the initial tests show isolated canting with high resulting forces, the angular range is restricted to $\pm 12.5°$. The range of possible compensatable angles will be checked later on the experimental setup in Section 4 by carrying out tests.

Table 1 Pluggability analysis of a CCS inlet and Combo 2 connector for translational and rotational deviations

Deviation	*Tolerance +/–*
Δx in [mm]	3/3
Δy in [mm]	5/5
$\Delta\theta_x$ in [°]	7.6/13
$\Delta\theta_y$ in [°]	17/17
$\Delta\theta_z$ in [°]	9/9

The elastic compensation unit is located behind the head and is presented in Figure 2(a) from side and a sectional view is shown in Figure 2(c). The flexible part (pink) is hexagonal and is fixed in the housing. In this way the rotation around the z-axis is prevented and the compensation unit acts as a torsion spring. The design has cut outs for translational movement to the side and in the height of ± 5 mm. These cut outs also allow an angular compensation of $\pm 12.5°$. For the first prototype, the elastic compensation unit is 3D-printed out of the *SaintSmart: Flexible Filament* TPU with a hardness of 95 Shore A.

The mechanical structure and the actuators are dimensioned by taking into consideration (Deutsches Institut für Normung, 2012) (16.15) and to achieve a plug in force of 200 N. The plug in force is over dimensioned by a factor of 2, so that the forces required to deform the compensation unit are taken into account. Figure 7 in Section 4 shows the robot workspace in the yz-plane. The shoulder axis is located close to the wall ($z = 0$ mm) and is shown as a red cross. In the green area, the robot can be positioned with an horizontal aligned connector. Different vehicles can be charged by the charging robot. Depending on the inlet height of the vehicle, it has to be positioned at different distances from the wall in front of the charging robot. At a height of 750 mm the largest possible distance range is covered. This height is chosen based on the test vehicle used within the research project. However, the operating height can be adapted by adjusting the mounting height on the wall. Parallel to the vehicle (x-direction) the robot covers a distance of 600 mm.

The electric vehicle supply equipment (EVSE) can either be installed next to it as an external wallbox or can be integrated into a larger housing.

Figure 3 Modified connector and inlet, (a) modified connector: i – micro switch and ii – endoscope camera with IR-pass filter (b) inlet modification and position of the IR-LEDs (see online version for colours)

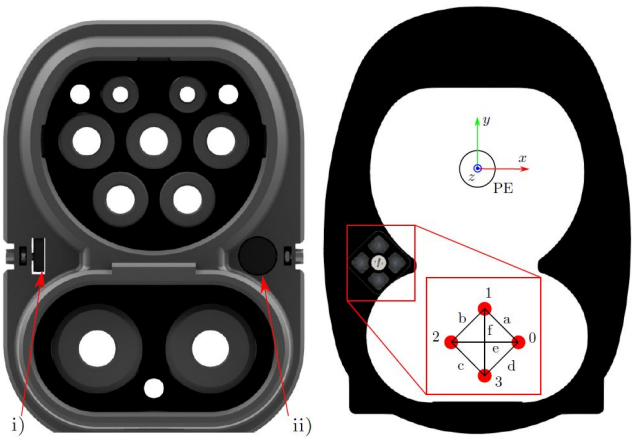

(a) (b)

3 Robot control scheme

The robot control is implemented in the Robot Operating System (Version Melodic Morenia on Ubuntu 18.04) developed by Stanford Artificial Intelligence Laboratory et al. (2016). The control unit communicates with the motor drivers via CANopen. Information obtained from image processing is used for tool center point (TCP) velocity control. For image acquisition, it is used a Ø8 mm endoscope camera (VOLTCRAFT VC-8919590) with a resolution of 640 × 480 pixel for a video with 30 frames per second (FPS). The camera uses a CMOS 1/6 inch camera sensor and has a focus range of 30–60 mm. Even so the focus covers only a small range, the accuracy

requirement is highest when the connector is in the focus range close to the inlet. In front of the camera an IR pass filter is mounted. The IR pass filter blocks the main proportion of the radiation below 850 nm. Hence the main part of the terrestrial solar radiation is not visible in the camera image. The camera is calibrated with the mounted IR pass filter using an x by y IR-LED grid pattern. Figure 3(a) shows a micro switch i mounted in the connector, which is used as an end stop during plugging. In addition, the camera position in the connector with the IR pass filter in front of it can be seen. The camera is located between the AC and DC part of the connector, because, according to DIN 62196-3, it is not allowed to cover the space at the sides and directly above the connector. Figure 3(b) illustrates the markers arrangement with four Ø3 mm IR-LEDs (940 nm) covered by a projection screen. The markers are recessed in the inlet to ensure clearly defined round markers. To make the markers visible at inclined viewing angles, a projection screen is used. By positioning the camera inside the connector and the markers at the same position on the opposite side, it can be ensured that the markers are detected during the entire visual servoing process. Thus, the robot never moves 'blind'. The marker layout is designed in a way, that one LED is located directly in front of the camera during the charging process and can serve as an additional communication opportunity, if the WLAN connection is interrupted. To calculate the pose, the PnP problem has to be solved. There exist solutions for at least three points, but for a unique solution, a minimum of four points are necessary. For example, if the P3P algorithm of Persson and Nordberg (2018) is used, two solutions result from the marker arrangement, which differ in the sign of the angle around the x-axis. Therefore, four markers in form of IR-LEDs are used. A pose estimation using these markers is implemented and is explained later on. As soon as the vehicle requests the charging process via WLAN connection, the process proceeds in the steps shown in Figure 4.

3.1 Searching markers parallel to the vehicle

First, the charging robot is looking for the LEDs and is trying to estimate a rough position. To do this, it moves along the linear axis and looks for the inlet with the illuminated LED pattern. The centre points of the LEDs are obtained with blob detection in the camera image. A blob is an area of an image with similar grey levels. If four blobs are detected, their pattern has to be checked for plausibility independent of scaling and rotation. Because of the blob detection various other elements are also identified resulting in a set of centre points $\mathbf{b}_i \in \mathcal{B}$ with possible $\#\mathcal{B} \geq 4$. A preselection is made by defining a minimal grey level $g_{\min}$ and an ellipsoid shape precision of 85% as defined by Marchand and Chaumette (2005).

If $\#\mathcal{B} > 4$ still holds, the most plausible blob set is chosen based on the ratios between the centre point distances of the desired LED markers and the detected blobs. This measure for the plausibility check is based on Wissing et al. (2015).

Figure 4 Charging procedure: 1 – parallel to vehicle, 2 – start configuration, 3 – visual servoing and 4 – plugging/unplugging (see online version for colours)

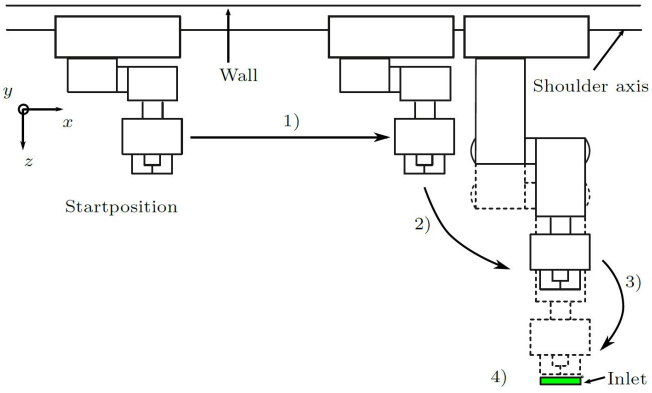

Table 2 Coordinates of the LED-markers ${}^{o}\mathbf{B}_i$

LED-number	${}^{o}\mathbf{B}_i({}^{o}X_i, {}^{o}Y_i, {}^{o}Z_i)$ *in [m]*
0	(0, 0, 0)
1	(–0.0052, 0.0052, 0)
2	(–0.0104, 0, 0)
3	(–0.0052, –0.0052, 0)

The coordinates of the LED-markers ${}^{o}\mathbf{B}_i$ with respect to the object frame are listed in Table 2 and for the reference distances follows $l^*_{ij} = \|{}^{o}\mathbf{B}_j - {}^{o}\mathbf{B}_i\|$. The centre points in the image plane are transformed from pixel units to metres using the set of camera intrinsic parameters $\mathbf{a} = (u_0, v_0, p_x, p_y)$, which are obtained from camera calibration. u_0 and v_0 are the coordinates of the principal point in pixel. p_x and p_y are the ratio between the focal length and the size of a pixel.

The distances between two detected blob centre points $\mathbf{b}_i$, $\mathbf{b}_j$ in the image plane are defined by $l_{ij} = \|\mathbf{b}_j - \mathbf{b}_i\|$. The ratios r_i are calculated for every subset $\mathbf{b}_{mnoq} = \{\mathbf{b}_m, \mathbf{b}_n, \mathbf{b}_o, \mathbf{b}_q\} \subseteq \mathcal{B}$ containing four unique blob centre points (indices: m, n, o, q) out of all detected blobs.

$$\mathbf{b}_{mnoq} = \{\{\mathbf{b}_m, \mathbf{b}_n, \mathbf{b}_o, \mathbf{b}_q\} | \{\mathbf{b}_m, \mathbf{b}_n, \mathbf{b}_o, \mathbf{b}_q\} \subseteq \mathcal{B} \wedge m \neq n \neq o \neq q\} \tag{1}$$

To check each subset $\mathbf{b}_{mnoq}$ for plausibility four length ratios

$$r_1(\mathbf{b}_{mnoq}) = \frac{\frac{l_{mq}}{l_{mn}} \cdot \frac{l_{mo}}{l_{mn}}}{\frac{l^*_{03}}{l^*_{01}} \cdot \frac{l^*_{02}}{l^*_{01}}}, \quad r_2(\mathbf{b}_{mnoq}) = \frac{\frac{l_{mn}}{l_{no}} \cdot \frac{l_{oq}}{l_{qn}}}{\frac{l^*_{01}}{l^*_{12}} \cdot \frac{l^*_{23}}{l^*_{31}}}$$
$$r_3(\mathbf{b}_{mnoq}) = \frac{\frac{l_{no}}{l_{oq}} \cdot \frac{l_{mo}}{l_{mn}}}{\frac{l^*_{12}}{l^*_{23}} \cdot \frac{l^*_{02}}{l^*_{01}}}, \quad r_4(\mathbf{b}_{mnoq}) = \frac{\frac{l_{oq}}{l_{qm}} \cdot \frac{l_{oq}}{l_{qn}}}{\frac{l^*_{23}}{l^*_{30}} \cdot \frac{l^*_{23}}{l^*_{31}}} \tag{2}$$

are used. The numerator contains the length ratios between the detected blobs in the image. The denominator contains the corresponding ratios of lengths between the desired

marker coordinates projected into the image plane. With these ratios a set plausibility p_s is defined by

$$p_s(\mathbf{b}_{mnoq}) = \frac{1}{4}\sum_{i=1}^{4} 1 - |1 - r_i(\mathbf{b}_{mnoq})|. \tag{3}$$

Following the most plausible subset $\mathbf{b}^*_{mnoq}$ is chosen as

$$\mathbf{b}^*_{mnoq} = \{\mathbf{b}_{mnoq} | p_s(\mathbf{b}_{mnoq}) = \max_{\forall \mathbf{b}_{mnoq}} (p_s(\mathbf{b}_{mnoq})) \wedge p_s(\mathbf{b}_{mnoq}) > 0.9\}. \tag{4}$$

The threshold for the plausibility measure has to be at least 90%. This value is selected, because from a large distance, the errors from the marker position detection can reduce the correct marker set's plausibility parameter. In addition, it is not possible to achieve 100% plausibility at the beginning if the inlet is tilted. Due to the projection into the image plane, the distances of the opposite blobs are shorter, which reduces the calculated plausibility measure. If the plausibility check was passed, the relative position of the connector to the input is calculated using the linear *Lagrange* approach for initialisation and the nonlinear *virtual visual servoing* approach for the following pose estimation. In order to ensure the convergence of the minimisation process with a nonlinear approach, a starting position through a linear approach is required. Both are implemented in the *VISP* library by Marchand et al. (2005) and they are described in detail by Project et al. (2012). Figure 5 shows the application of the blob detection, the plausibility check and the pose estimation. In Figure 5(a1) with the corresponding raw picture in Figure 5(a2), it is shown that the plausibility check is finding the correct four blobs corresponding to the LED markers. Hence the pose estimation is done right as it is displayed by the coloured coordinate system in LED-number 0. While the robot arm is moving forward to the inlet, the LEDs are detected correctly, as shown in Figures 5(b) and 5(c). The camera is at the corresponding position opposite LED 0, which is why it is moving towards point (0, 0) in the camera frame and heading for the origin of the displayed coordinate system.

The image is divided into grey levels for the blob detection. Initially, for the minimum grey level a low threshold of $g_{\text{min}} = 80$ is set for blob detection in order to be able to detect the LEDs from maximum distance as well. g_{min} is determined under laboratory conditions. After the first blob detection and the first pose estimation and passed plausibility check, the minimum grey level is adjusted depending on the distance dz in [m] using the following equation

$$g_{\text{min}} = 0.13 \cdot \frac{1}{dz^2} - 0.41 \cdot \frac{1}{dz} + 80. \tag{5}$$

Thus, the LEDs are detected even at short distances.

The procedure *searching markers parallel to the vehicle* is illustrated in Listing 1 in form of pseudo code. It can be seen that if the LEDs in form of blobs are successfully detected and the plausibility check is passed, the ACD is moving to the start configuration.

Figure 5 LED detection and pose estimation, (a) marker detection in the beginning (plausibility check) (b) detection halfway to inlet (c) detection just before plugging (see online version for colours)

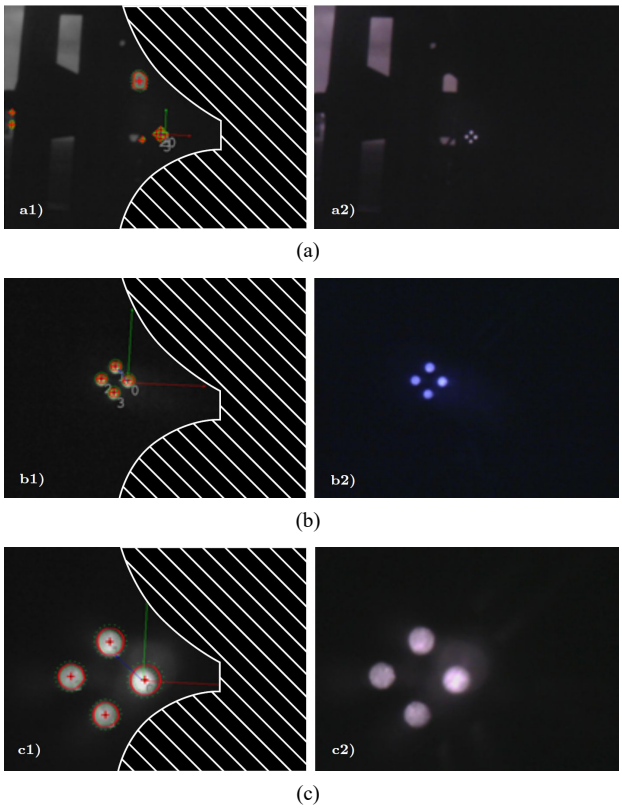

Listing 1 Pseudo code to search markers parallel to the vehicle

```
program Searching markers parallel to vehicle
  p_s = [p_s1, p_s2, ...] = [0, 0, ...]
  while max(p_s) < 0.9 and ACD is in boundaries do
    move ACD along x−axis (parallel to vehicle)
    detect blobs in camera image
    extract b_i ∈ B
    if #B ≥ 4
      for each b_mnoq
        calculate r_i
        calculate p_s
      end for
    else
      p_s = [0, 0, ...]
    end if
  end while
  if max(p_s) ≥ 0.9
    find b*_mnoq
    calculate inlet pose from b*_mnoq
    move ACD in Start configuration
  else
    move ACD in home position
  end if
end program Searching markers parallel to vehicle
```

3.1.1 Start configuration

If the pose estimation yields a position, which is possible for plugging, the pose estimation is used to perform a pilot control. This causes the robot to move point to point (PTP) 120 mm in front of the inlet. The connector's orientation remains straight ahead to avoid possible orientation errors within the pose estimation from the large initial distance.

3.1.2 ID check

After reaching the start configuration, a check is made to determine that the right vehicle is in front of the charging station. Relying only on wireless communication may result in a mismatch between the charging station and the EV. This makes visual identification of the EV necessary. A unique EVID is required for correspondence control, which is transmitted via WLAN and also by IR communication and then compared. The EV can use its marker IR-LEDs as a transmitter and the camera or an additional dedicated IR receiver can be used as a receiver on the charging station. For each charging session the EVID is a new randomly generated eight character string. When the camera is used, the ASCII encoded EVID is transmitted with one LED as the clock and a second one as the data signal. In this case LED 0 transmits the clock and LED 2 transmits the data signal. The bit rate is limited by the FPS of the camera, with a minimum of two frames per bit. A much higher bit rate is possible with a standalone IR receiver, but it requires additional hardware.

3.1.3 Visual servoing

The visual servoing starts after the ID check. As a safety feature, the ACD only moves when all four LEDs are detected and pass the plausibility check. Otherwise the robot stops, tries to find the markers again or after a few seconds it moves back to its home position. This ensures that there is no obstacle between the ACD and the vehicle during visual servoing. For visual servoing a *2 1/2D visual servoing* approach is used as described by Malis et al. (1999) and is shown in Figure 6. In order to determine the necessary movement speeds of the robot arm, the angular and translational deviations are considered separately. The following control law for the origin velocity of the camera frame $\mathbf{v}_c(\mathbf{t}_c, \boldsymbol{\omega}_c)$ has to be solved finally.

$$\mathbf{v}_c = -\lambda(|\mathbf{e}|)\widehat{\mathbf{L}}^{-1}\mathbf{e} \tag{6}$$

The error $\mathbf{e}$ contains the position error and the orientation error $\mathbf{e} = [\mathbf{d} - \mathbf{d}^*, \mathbf{u}\theta - \mathbf{u}\theta^*]^\top$. $\mathbf{u}$ are the rotation axes and θ is the angle obtained from the rotation matrix $\mathbf{R}$ between the desired and the current camera frame. In order to be straight aligned in front of the inlet, $\mathbf{R}$ has to become the identity matrix. Hence $\mathbf{u}\theta^*$ has to be 0. The values to be determined are calculated relying on the previous pose estimation (see Figure 6). $\lambda(|\mathbf{e}|)$ is an adaptive gain depending on the amount of the error $\mathbf{e}$. It is implemented in *VISP*. $\widehat{\mathbf{L}}^{-1}$ is the approximation of the inverse interaction matrix $\mathbf{L}^{-1}$.

As shown in Figure 6, the translational velocities $\mathbf{t}_c$ and the rotational velocities $\boldsymbol{\omega}_c$ are transmitted to the robot controller afterwards.

Figure 6 Block diagram of the 2 1/2D visual servoing based on Malis et al. (1999) (see online version for colours)

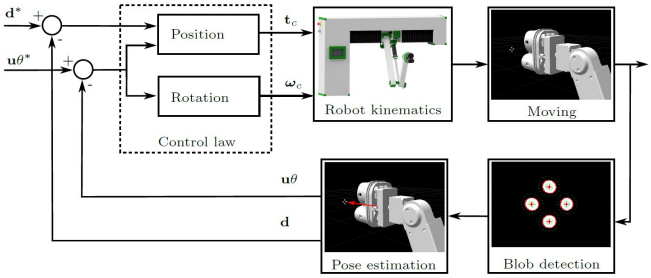

Table 3 Target and accuracy goal of visual servoing

Error **e**	*Target (*)*	*Accuracy*
d_x	0 mm	±2 mm
d_y	0 mm	±2 mm
d_z	55 mm	±2 mm
θ_x	0°	±2.5°

The visual servoing is finished when the error $\mathbf{e}$ is within the ranges shown in Table 3. According to this, the target is perfectly aligned to be 55 mm in front of the inlet. The distance of $d_z = 55$ mm is chosen leaving a gap of 6.6 mm between the connector and the inlet. This gap prevents collisions during the visual servoing. The accuracy is sufficient for successful plugging based on the pluggability analysis in Table 1. In addition, the target pose is at the border of the cameras focus range.

To ensure that the accuracy of visual servoing is sufficient, an error assessment of the pose estimation based on the intrinsic camera parameters $\mathbf{a}$ is calculated. This is done by determining how the pose changes if the detected blobs centres deviates by one pixel in both directions in the image plane. For the nonlinear *virtual visual servoing* approach for pose estimation, a lambda of $1 \cdot 10^{-4}$ is selected. The maximum deviations due to the displacement of the image coordinates of the marker centres are listed in Table 4. This shows that the camera accuracy and the pose estimation is for the translational axes x and y and for the rotational axis around x higher than the accuracy required by the visual servoing. Only in the z-axis the maximum possible error could be up to 4.4 mm. This error can be neglected if the connector is aligned with sufficient accuracy, since there is a linear plugging movement.

Table 4 Camera and pose estimation accuracy with maximum pose error

Axis	*Maximum error*
x	0.19 mm
y	0.12 mm
z	4.4 mm
θ_x	0.31°

3.1.4 Plugging

The final plugging is done with a Cartesian path control using the current orientation of the compensation unit as the direction. It is assumed that the connector and the compensation unit are aligned. A linear plugging movement is executed until the micro switch in the connector detects a contact.

3.1.5 Unplugging and homing

After the vehicle has been charged, the charging robot unplugs in the same Cartesian path as the plug in process. Afterwards the robot moves back to its home position in PTP control.

4 Experiments and results

4.1 Workspace evaluation

To evaluate the performance of the ACD, plugging experiments are performed in a laboratory environment. The modified inlet is positioned at several positions in the robot workspace, resulting in an evenly distributed grid with 100 mm spacing. The test plan is shown in Figure 7 with the experimental setup in Figure 8. For the different inlet poses a fixable cardanic suspension is designed to rotate the inlet around the tip of the PE-pin. The x-axis is neglected in the experimental design, because it has a one-to-one mapping of one DOF regarding to the linear robot axis. Therefore, no interactions with the inlet position in other spatial directions are expected. The inlet is tilted around the x-axis of the inlet [see Figure 3(b)] in steps of 7.5° in a range of –15° to 15°, displayed as red vectors in Figure 7. A position is considered as pluggable, if a point 150 mm in front of the inlet is still in the workspace so that the robot can reach the start position for the visual servoing. Non-pluggable positions are eliminated from the test plan. The goal of the first test series is the evaluation in which workspace the inlet-detection works and if the developed robot control scheme is sufficient. In addition, it can be evaluated whether the pose estimation with the four IR markers also works in different angular orientations reliably and whether the robot positions itself in front of the inlet correctly.

All test series are carried out under laboratory conditions at a temperature of 22°C as constant as possible and under the same indoor light conditions. Tables 5 to 9 show the results of the first test series. The EVs angle (θ_{yaw}) or equivalent to θ_y in relation to the inlet coordination system shown in Figure 3(b) is 0°. Only the inlet tilt angle θ_x can be actively controlled by the ACD, as described in Section 2. θ_x varies depending on the car manufacturer and even within a single manufacturer's model range. The test results show that plugging at an inlet height of 950 mm (10 mm below the shoulder axis) is only achieved at an inlet tilt of θ_x = 15° and as well only in three out of five attempts. Those errors occur because of an inaccurate initial pose estimation, when the robot arm tries to move to a start position that it cannot reach. Otherwise, the other results show that a reachable inlet, which is tilted within the range of $-7.5° \leq \theta_x \leq 7.5°$, can be plugged in at least 96% of attempts. Only isolated attempts in the boundary area of the workspace failed, in which the robot looses the markers during visual servoing. If the pose estimation at the beginning and the associated PTP positioning is not sufficiently central in front of the inlet, the visual servoing will fail. One reason for this is the camera position between the connector's AC and DC part, which limits the field of view as seen in Figure 5. As it is shown in Table 8 the inlet positions close to the robot (z = 450, z = 550) cannot be plugged. This is because the head reaches its position limit. It occurs at very close inlet positions, so the DOF in y-direction is missing at the beginning of the workspace. No problems occur with slightly tilted inlets (see Tables 5 and 7), so that plugging tests were successful.

Figure 7 Test points – *red vectors* – positioned in the workspace with θ_{yaw} = 0° (see online version for colours)

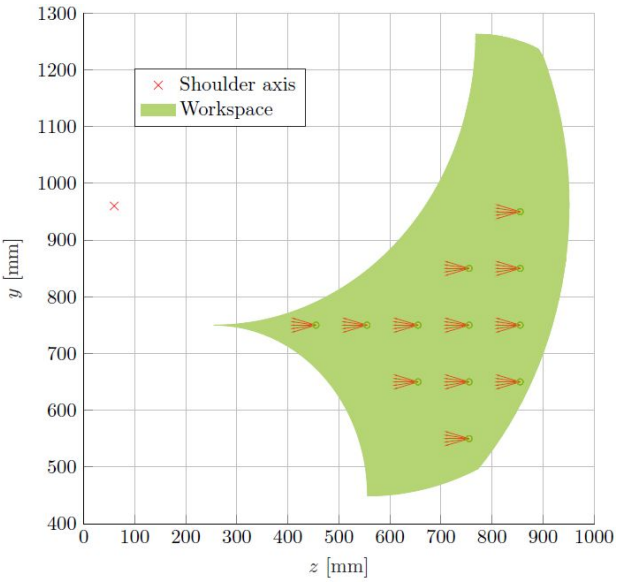

Figure 8 Experimental setup (see online version for colours)

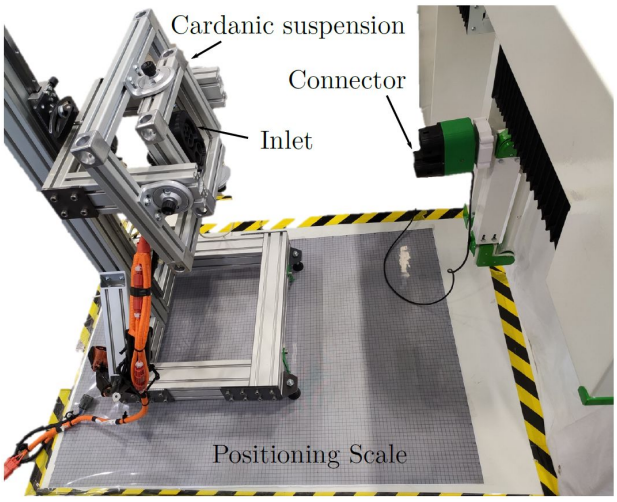

Table 5 $\theta_x = 0°$ and $\theta_y = 0°$ (see online version for colours)

y \ z	450	550	650	750	850
950	\	\	\	\	0/5
850	\	\	\	5/5	5/5
750	5/5	5/5	5/5	5/5	5/5
650	\	\	5/5	5/5	5/5
550	\	\	\	4/5	\

Table 6 $\theta_x = -7.5°$ and $\theta_y = 0°$ (see online version for colours)

y \ z	450	550	650	750	850
950	\	\	\	\	0/5
850	\	\	\	5/5	5/5
750	0/5	5/5	5/5	5/5	5/5
650	\	\	5/5	5/5	4/5
550	\	\	\	5/5	\

Table 7 $\theta_x = 7.5°$ and $\theta_y = 0°$ (see online version for colours)

y \ z	450	550	650	750	850
950	\	\	\	\	0/5
850	\	\	\	5/5	5/5
750	5/5	5/5	5/5	5/5	4/5
650	\	\	5/5	5/5	4/5
550	\	\	\	5/5	\

Table 8 $\theta_x = -15°$ and $\theta_y = 0°$ (see online version for colours)

y \ z	450	550	650	750	850
950	\	\	\	\	0/5
850	\	\	\	4/5	4/5
750	0/5	0/5	5/5	5/5	5/5
650	\	\	5/5	5/5	5/5
550	\	\	\	5/5	\

Table 9 $\theta_x = 15°$ and $\theta_y = 0°$ (see online version for colours)

y \ z	450	550	650	750	850
950	\	\	\	\	3/5
850	\	\	\	2/5	3/5
750	0/5	5/5	5/5	3/5	2/5
650	\	\	0/5	3/5	0/5
550	\	\	\	0/5	\

Even though an inlet tilt of $\theta_x = 15°$ is rather unlikely for ergonomic reasons, it is analysed in this case. In Table 9, it can be seen that the lower parts of the workspace can hardly be detected when the inlet is tilted downwards. In addition, there are a lot of failed attempts in which the robot looses the markers during visual servoing. Since this only occurs more frequently with large positive angular inclinations, this error is clearly due to the reduced field of view because of the connector's DC part. Since the start configuration is approached only using three DOFs and afterwards the robot has to tilt the connector upwards (with positive inlet tilt), the robot looses the markers earlier than if the connector is tilted downwards. This is due to the wider and longer DC part of the connector [see Figure 2(a)], which significantly reduces the camera's view downwards.

Isolated tests show that it is possible to plug in an upward tilt of $\theta_x < -15°$, but the area that can be plugged is smaller. Due to the large tilt, the robot can reach its position limit at the head (head mount contacts the forearm), so that plugging is only possible in the lower area of the workspace and only at distances $\geq$650 mm.

In total, 300 tests were performed and 225 out of them were successful. This results in a success rate of 75%. If the positions with 0/5 successful plugging attempts are excluded (fail in pose estimation or position limit of robot mechanics during the visual servoing), the success rate increases to 92%. In the test area of $\theta_x < 7.5°$ the success rate increases to 97%.

4.2 Compensation unit evaluation

The second test series examines, in which area the elastic compensation unit works successfully. The different angular positions θ_x, θ_y and θ_z are adjusted on the cardanic suspension (see Figure 8). Pretests with $\theta_x = 0°$ have shown that orientations with θ_z in the range $-6° \leq \theta_z \leq 6°$ can be plugged several times in a row. For θ_y a range of $-7.5° \leq \theta_y \leq 7.5°$ is determined. For the following test series, the inlet tilt around the x-axis is also varied in the range of $-7.5 \leq \theta_x \leq 7.5$ in order to be able to analyse all mutual interactions.

Table 10 $\theta_x = 0°$ (see online version for colours)

θ_y \ θ_z	−6°	0°	6°
−7.5°	5/5	5/5	5/5
0°	5/5	5/5	5/5
7.5°	5/5	5/5	5/5

Table 11 $\theta_x = -7.5°$ (see online version for colours)

θ_y \ θ_z	−6°	0°	6°
−7.5°	0/5	5/5	5/5
0°	5/5	5/5	5/5
7.5°	0/5	5/5	5/5

Table 12 $\theta_x = 7.5°$ (see online version for colours)

θ_y \ θ_z	−6°	0°	6°
−7.5°	5/5	5/5	5/5
0°	5/5	5/5	5/5
7.5°	5/5	5/5	5/5

Tables 10 to 12 show the results of the second test series. In summary, all investigated inlet poses except of two can

be plugged successfully. For theta $\theta_x = 0°$ and $\theta_x = 7.5°$ a 100% success rate can be achieved in the variation range of θ_y and θ_z. No successful plugging can be achieved for the two inlet orientations ($\theta_x = –7.5°$, $\theta_y = –7.5°$, $\theta_z = –6°$) and ($\theta_x = –7.5°$, $\theta_y = 7.5°$, $\theta_z = –6°$). The connector enters the inlet, but is canted and cannot be fully inserted.

4.3 Reaction forces

To determine the reaction forces on the inlet, a six-axis load cell (K6D68 1 kN/20 Nm from ME Meßsysteme GmbH) is installed between the suspension and the inlet. For the force measurement, it is important to note that the connector as well as the front part of the inlet are 3D printed prototypes. Due to inaccuracies in printing and rougher surfaces, higher forces are expected. In addition, no electrical contacts are installed in the connector, so that the forces are not comparable with common used connectors quantitatively. Nevertheless, initial force measurements provide qualitative information about the reaction forces when using the elastic compensation unit.

Figure 9 Measured reaction forces on the inlet while plugging at inlet orientation $\theta_x = \theta_y = \theta_z = 0°$ (see online version for colours)

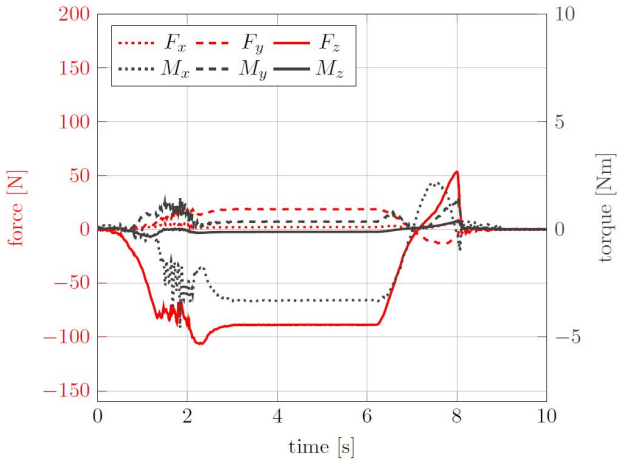

Figure 10 Measured reaction forces on the inlet while plugging at inlet orientation $\theta_x = –7.5°$, $\theta_y = –7.5°$, $\theta_z = 0°$ (see online version for colours)

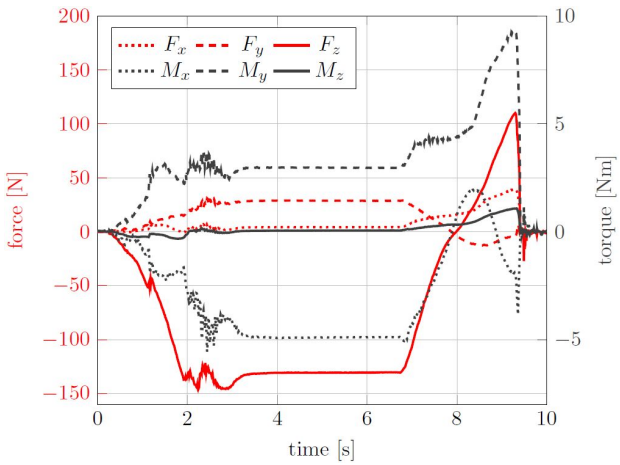

Figures 9 and 10 show the forces F_x, F_y, F_z and the torques M_x, M_y and M_z in relation to the inlet coordinate system [Figure 3(b)] for the inlet orientations $\theta_x = \theta_y = \theta_z = 0°$ and $\theta_x = –7.5°$, $\theta_y = –7.5°$, $\theta_z = 0°$. No elastic compensation is required for the first inlet pose, whereas the second one needs elastic compensation around the y-axis. θ_x is $\neq 0$ to see any interactions between the orientations around the x-axis and the y-axis. Plugging is done within the first three seconds, followed by a waiting time of 3 s with final unplugging. The force measurements lead to the observations:

- In case of plugging as well as unplugging, the force F_z increases considerably, if the elastic compensation unit is required. The higher forces can possibly be attributed to the reaction forces on the inlet walls caused by friction. In addition, a significant increase in the reaction torque M_y can be seen, which is caused by the elastic compensation around the y-axis. During unplugging, the torque M_y increases to a maximum, which indicates that the connector is canted in the inlet.
- In both tests, M_x is considerably high, what can be attributed to slight errors in the pose estimation just before plugging. This can result in slight canting and slipping, as can be seen in the force F_z (jittering in force measurement). The jitter is possibly a manifestation of the *stick-slip phenomenon*.
- As expected, the forces F_x and F_y are almost identical in both tests. In these x, y-dimensions a sufficiently accurate positioning is achieved.

5 Discussion

The test series show several positive and negative aspects of the developed ACD. As seen in the workspace evaluation the charging procedure works reliably and it can be plugged successfully in most cases. Some inlet poses cannot be plugged, because the camera looses the markers during visual servoing. The investigations show that due to the camera position in the connector a large field of view is shaded by the connector's AC and DC part. This shortcoming could be solved by a two-step visual servoing, if the first visual servoing only sets the correct orientation at a larger distance. Better suited camera positions at the front or on the outside of the connector are not permitted by the above mentioned standard. If the inlet poses are neglected, which are not achieved in this way, the charging robot plugs successfully at a rate of at least 92% within the analysed workspace.

The compensation unit evaluation shows that the elastic compensation unit works in the investigated region. The series also show that the inlet pose was repeatably plugged five out of five times. Only two inlet poses cannot be plugged successfully. Even if the connector is inserted halfway into the inlet, the connector is getting canted in the inlet and the forces and torques increase to an unacceptable

level. Why these two poses cannot be plugged, cannot be exactly concluded from the available data, especially because the corresponding poses with $\theta_z = 6°$ were plugged successfully. Since these poses are at the limit of possible angular compensation, aspects such as surface deviations, manufacturing tolerances or anisotropic effects in the 3D-printed compensation unit, can lead to canting in an orientation while a symmetrical setup could be plugged in. Further research is necessary to identify and remedy the cause of canting.

Based on the force measurements, it can be determined that the use of the developed elastic compensation unit causes an increase in force and torque that cannot be neglected. The high forces and torques can be caused by a too stiff compensation unit. That makes further investigations necessarry. The measurements also show that the torque M_x increases with changes of orientation around the y-axis. This can only be due to inaccuracies of the robot positioning in front of the inlet. These slight deviations can lead to canting during plugging, which results in high forces and torques.

However, the experiments show that the low-cost robot can achieve a repeatable plugging. The system with a camera in the connector allows a very close positioning in front of the inlet, so that the accuracies of the camera, the pose estimation and the visual servoing are decisive for a successful plugging. The accuracy and stiffness of the presented charging system cannot be compared with those of an expensive industrial robot. But they are sufficient for plugging. Inaccuracies in the robot mechanics and misalignments between the compensation unit and the connector can be elastically compensated. This will also result in a higher plugging force and a recording of momentum.

With temperature changes, the mechanic properties of the compensation unit will change. It is expected that with lower temperatures the spring rate will increase, resulting in higher reaction forces. Higher temperatures decrease the stiffness, possibly causing sagging of the connector under static gravity load. Due to the visual servoing slight sagging need not result in failure. With increasing number of pluggings ageing of the compensation unit will occur. The ageing and a possible layer separation of the 3D-printed TPU component can also result in sagging and a reduced stiffness.

6 Conclusions and future work

This paper presented the development of a low-cos ACD for the CCS Combo 2 connector with only four DOFs (three translational and one rotational) designed for usage in public areas, while taking safety into account. An elastic compensation unit was constructed for the missing two DOFs, which is installed between the robot arm and the connector. The compensation unit is dimensioned and designed on the basis of a pluggability analysis for translational and rotational deviations between the CCS inlet and the connector. As markers IR-LEDs were installed in the vehicle inlet for the robot control scheme, so that the robot is able to find the inlet with a low-cost endoscope camera and an IR-pass filter mounted inside the connector. A plausibility check was used to reliably identify the four blobs in the image plane that correspond to the LED marker pattern. In addition, an identification check was carried out by pulsing the LEDs, which makes it possible to ensure that the correct EV and charging station are getting paired. Finally, the control system includes a visual servoing for which the necessary accuracies were defined on the basis of a pluggability analysis. Additionally, the camera selection was checked against an error estimation. By using the elastic compensation unit, the accuracy of the charging robot has less influence than an accurate visual inlet pose estimation. The designed ACD and the developed control scheme were tested and evaluated in various tests. Within the workspace evaluation a major part could be successfully plugged with a success rate of up to 97%. Boundary areas in the investigated workspace could not be successfully plugged. The compensation unit was evaluated in the range of $\pm 7.5°$ around the y-axis and $\pm 6°$ around the z-axis. Except for two poses, all investigated angular errors could be compensated. So the robot design with the elastic compensation unit and the control scheme can be classified as working. Due to the 3D printed prototypes for connector and the front cover of the inlet, the force measurements could only provide qualitative results, but showed that various force increases occur due to slight positioning errors of the connector and that the positioning accuracy still needs improvement. Finally, it was discussed that both the environmental temperature and the number of pluggings probably have an influence on the elastic compensation unit.

In further studies, the elastic compensation unit will be optimised in order to increase the effective workspace and to reduce the required plugging force. Furthermore, different image processing approaches will be evaluated for inlet pose estimation accuracy. In addition, the robot will be tested in various situations to determine how robust the system is against external environmental influences.

Acknowledgements

We gratefully acknowledge financial support through the German Space Agency (DLR) with funds provided by the German Federal Ministry for Economic Affairs and Energy (BMWi) due to a decision of the German Bundestag under Grant No. 01MV180014 (ALaPuN). The authors are responsible for the content of this publication.

References

Bay, H., Ess, A., Tuytelaars, T. and Van Gool, L. (2008) 'Speeded-up robust features (SURF)', *Computer Vision and Image Understanding*, Vol. 110, No. 3, pp.346–359, DOI: 10.1016/j.cviu.2007.09.014.

Behl, M., DuBro, J., Flynt, T., Hameed, I., Lang, G. and Park, F. (2019) 'Autonomous electric vehicle charging system', in *2019 Systems and Information Engineering Design Symposium (SIEDS)*, Charlottesville, VA, USA, pp.1–6, DOI: 10.1109/SIEDS.2019.8735620.

Bergmann, T. (2015) *Fangraumanalyse zur Beurteilung eines Stecksystems*, Unpublished Seminar paper, TU Dortmund University, Dortmund, Germany.

CarLa (2018) [online] *Volkswagen AG: CarLa Charges the Car* [online] https://www.volkswagenag.com/en/news/stories/2018/03/karla-charges-the-car.html (accessed 16 October 2020).

DAZEPLUG (2019) [online] *DAZEPLUG: Automatic Charger for Electric Vehicles* [online] https://www.dazetechnology.com/dazeplug/ (accessed 30 August 2021).

Deutsches Institut für Normung (2012) *DIN EN IEC 62196-3: Plugs, Socket-Outlets, and Vehicle Couplers – Conductive Charging of Electric Vehicles*.

Easelink (2020) [online] *Easelink Matrix Charging* [online] https://easelink.com (accessed 30 August 2021).

Electrify America (2019) [online] *Electrify America and Stable Announce Collaboration to Deploy Robotic Fast-Charging Facility for Self-Driving Electric Vehicle Fleets* [online] https://media.electrifyamerica.com/en-us/releases/70 (accessed 16 October 2020).

EVAR (2018) [online] *Samsung's Robot Charging Unit EVAR (Video)* [online] https://www.electrive.com/2018/09/19/samsungs-robot-charging-unit-evar-video/ (accessed 16 October 2020).

Harik, E. (2021) 'Design and implementation of an autonomous charging station for agricultural electrical vehicles', *Applied Sciences*, Vol. 11, No. 13, Article ID 6168, DOI: 10.3390/app11136168.

Innogy SE (2019) [online] *Roboter Zeigt Automatisches Schnellladen* [online] https://www.next-mobility.de/roboter-zeigt-automatisches-schnellladen-a-797275/ (accessed 16 October 2020).

KUKA CarLa Connect (2020) [online] *KUKA Carla Connect: Charging Robot for Electric Vehicles* [online] https://www.red-dot.org/project/kuka-carla-connect-45874 (accessed 30 August 2021).

Lou, Y. and Di, S. (2020) 'Design of a cable-driven auto-charging robot for electric vehicles', *IEEE Access*, Vol. 8, pp.15640–15655, DOI: 10.1109/ACCESS.2020.2966528.

Lv, X., Chen, G., Hu, H. and Lou, Y. (2019) 'A robotic charging scheme for electric vehicles based on monocular vision and force perception', in *2019 IEEE International Conference on Robotics and Biomimetics (ROBIO)*, Dali, China, pp.2958–2963, DOI: 10.1109/ROBIO49542.2019.8961689.

Mönnig, A., Schneemann, C., Weber, E., Zika, G. and Hemrich, R. (2019) *Electromobility 2035 – Economic and Labour Market Effects through the Electrification of Powertrains in Passenger Cars*, IAB-Discussionpaper Institute for Employment Research (IAB), No. 8/2019 [online] http://hdl.handle.net/10419/204855 (accessed 30 August 2021).

Malis, E., Chaumette, F. and Boudet, S. (1999) '2 1/2D visual servoing', *IEEE Transactions on Robotics and Automation, Institute of Electrical and Electronics Engineers (IEEE)*, Vol. 15, No. 2, pp.238–250, DOI: 10.1109/70.760345.

Marchand, E. and Chaumette, F. (2005) 'Feature tracking for visual servoing purposes', *Robotics and Autonomous Systems, Special issue on Advances in Robot Vision*, Vol. 52, No. 1, pp.53–70.

Marchand, E., Spindler, F. and Chaumette, F. (2005) 'ViSP for visual servoing: a generic software platform with a wide class of robot control skills', *IEEE Robotics and Automation Magazine*, Vol. 12, No. 4, pp.40–52, DOI: 10.1109/MRA.2005.1577023.

Miseikis, J., Rüther, M., Walzel, B., Hirz, M. and Brunner, H. (2017) '3D vision guided robotic charging station for electric and plug-in hybrid vehicles', Paper presented at *OAGM/AAPR & ARW Joint Workshop 2017*, Wien, Austria.

Pan, M., Sun, C., Liu, J. and Wang, Y. (2020) 'Automatic recognition and location system for electric vehicle charging port in complex environment', *IET Image Processing*, Vol. 14, pp.2263–2272, DOI: 10.1049/iet-ipr.2019.1138.

Pérez, J., Nashashibi, F., Lefaudeux, B., Resende, P. and Pollard, E. (2013) 'Autonomous docking based on infrared system for electric vehicle charging in urban areas', *Sensors*, Vol. 13, No. 2, pp.2645–2663, DOI: 10.3390/s130202645.

Persson, M. and Nordberg, K. (2018) 'Lambda twist: an accurate fast robust perspective three point (P3P) solver', in *Proceedings of the European Conference on Computer Vision (ECCV)*, Munich, Germany, pp.334–349, DOI: 10.1007/978-3-030-01225-0_20.

Petrov, P., Boussard, C., Ammoun, S. and Nashashibi, F. (2012) 'A hybrid control for automatic docking of electric vehicles for recharging', in *2012 IEEE International Conference on Robotics and Automation*, Saint Paul, MN, USA, pp.2966–2971, DOI: 10.1109/ICRA.2012.6225087.

Phoenix Contact GmbH & Co. KG (2020) [online] *DC Charging Cable* [online] https://www.phoenixcontact.com/online/portal/pi? (accessed 16 October 2020).

Project, L., Chaumette, F., Marchand, E., Spindler, F., Tallonneau, R. and Yol, A. (2012) *ViSP 2.6.2: Visual Servoing Platform: Computer Vision Algorithms* [online] https://visp-doc.inria.fr/manual/visp-tutorial-computer-vision.pdf (accessed 30 August 2021).

Quan, P., Lou, Y., Lin, H., Liang, Z. and Di, S. (2021) 'Research on fast identification and location of contour features of electric vehicle charging port in complex scenes', *IEEE Access*, DOI: 10.1109/ACCESS.2021.3092210.

Stanford Artificial Intelligence Laboratory et al. (2016) *Robotic Operating System*, Version: ROS Kinetic Kame [online] https://www.ros.orguri=pxc-oc-itemdetail:pid=1408433&library=pien&tab=1 (accessed 16 October 2020).

Taraglio, S. (2017) *Robotised Fast Charging of Electric Buses*, Italian National Agency for New Technologies, Energy and Sustainable Economic Development, 5.1 Rapporto Tecnico ENEA [online] http://hdl.handle.net/20.500.12079/6767 (accessed 30 August 2021).

Walzel, B., Strum, C., Fabian, J. and Hirz, M. (2016) 'Automated robot-based charging system for electric vehicles', in *16th Internationales Stuttgarter Symposium*, Stuttgart, Germany, DOI: 10.1007/978-3-658-13255-2_70.

Wissing, C., Braun, J., Rösmann, C. and Betram, T. (2015) 'Control concept design for a robotic arm used for automatic charging', *Symposium Mechatronic 2015*, Dortmund, Germany, pp.31–36.